Electronic Supplementary Information (ESI) for Material Horizons.
This journal is © The Royal Society of Chemistry 2025

Electronic Supporting Information

High-Performance Dynamic Random Access Memory Capacitor with an Equivalent Oxide Thickness of 0.31 nm via Stepwise Cycling in Y-doped $Hf_{0.5}Zr_{0.5}O_2$ Thin Films

Jonghoon Shin,[a] Haengha Seo,[a] Janguk Han,[a] Tae Kyun Kim,[a] Heewon Paik,[a] Haewon Song,[a] Hansub Yoon,[a] Han Sol Park,[a] Kyung Do Kim,[a] Seong Jae Shin,[a] Jae Hee Song,[a] Sanghyup Lee,[a] Seungheon Choi,[a] Dong Hoon Shin,[a] Juneseong Choi,[a] and Cheol Seong Hwang*[a]

a Department of Materials Science and Engineering, and Inter-University Semiconductor Research Center, Seoul National University, Seoul, 08826, Republic of Korea.

* Corresponding author (e-mail: *cheolsh@snu.ac.kr*)

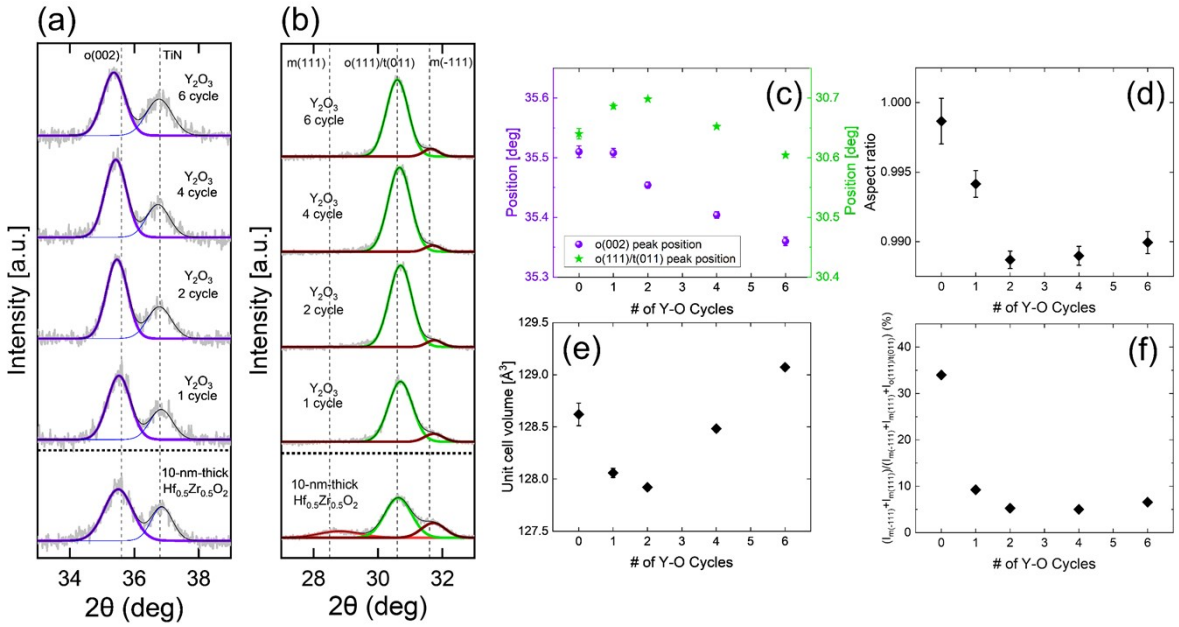

Figure S1. Background-subtracted GIXRD (incident angle: 0.5°) patterns (grey) of ~10-nm-thick $Hf_{0.5}Zr_{0.5}O_2$ films with varying numbers of Y_2O_3 IL ALD cycles inserted in the middle for (a) o(002) (purple) and TiN (blue) peaks (b) o(111)/t(011) (green), m(111) (red) and m(-111) (brown) peaks, and the cumulative results for the mentioned peaks (black), respectively. The (c) peak positions, (d) aspect ratio, (e) unit cell volume, and (f) m-phase areal ratio of the films. Error bars are included for the peak positions from the standard deviation of the Gaussian fitting. Error bars of the aspect ratio and unit cell volume are estimated from the error of the peak positions of the o(002) and o(111)/t(011) peaks. Reproduced with permission.[1] Copyright 2024, Royal Society of Chemistry.

Figure S1a,b show the background-subtracted GIXRD patterns and the Gaussian deconvoluted curves of ~10-nm-thick $Hf_{0.5}Zr_{0.5}O_2$ films with varying numbers of Y_2O_3 IL ALD cycles (zero, one, two, four, and six) inserted at the middle of the films after PMA at 525 °C for 30 seconds. Figure S1c shows the 2θ shifts of the deconvoluted o(002) and o(111)/t(011) peaks. According to Bragg's law, a decrease (or increase) in 2θ corresponds to an increase (or decrease) in the interplanar spacing. The o(002) peaks shifted monotonically to lower 2θ values with increasing Y_2O_3 IL cycles, attributed to the substitutional diffusion of larger Y^{3+} ions (90 pm) into the smaller Hf^{4+} and Zr^{4+} sites (72 pm), resulting in lattice expansion.[1] In contrast, the o(111)/t(011) peak shifted to higher 2θ values up to two ALD cycles, but decreased

monotonically at higher cycles, similar to the o(002) peak. Previous studies extensively reported that the 2θ position of the o(111)/t(011) peak is influenced not only by dopant-induced lattice expansion (or contraction), but also by variations in the relative phase fractions of the t- and PO-phases.[1-5] An increased t-phase (and decreased PO-phase) shifts this peak toward higher 2θ values[1-5], which may explain the observed discrepancy.

To confirm this, the AR and unit cell volume were presented in Figure S1d,e, respectively, calculated from the interplanar spacings d_{111} and d_{002} of the o(111)/t(011) and o(002) peaks, assuming negligible differences in the two shorter lattice constants. Further details regarding the calculation and assumptions can be found in previous studies.[1, 5, 6] The AR values decreased from zero to two Y_2O_3 ALD cycles, indicating the increased t-phase. At higher cycles, the AR values saturated, as Y diffusion was limited to regions near the IL and could not influence the phase changes in regions farther from the IL. The unit cell volume decreased up to two cycles but increased at higher cycles. This trend is attributed to the combined effects of phase transition and dopant-induced lattice expansion. At lower cycles, the reduction in unit cell volume was primarily driven by the increased t-phase. In contrast, at higher cycles, lattice expansion due to substitutional Y diffusion became dominant, as the phase transition effect had already saturated.[1]

Figure S1f shows the relative m-phase fraction changes calculated from $(I_{m(-111)} + I_{m(111)})/(I_{m(-111)} + I_{m(111)} + I_{o(111)/t(011)})$, where $I_{x(hkl)}$ denotes the areal intensity of the x(hkl) peak in the GIXRD pattern. Due to the higher PMA temperature (525 °C) in the previous study, the 10-nm-thick $Hf_{0.5}Zr_{0.5}O_2$ displayed a significant m-phase areal fraction of ~34%. In contrast, the Y_2O_3 inserted films exhibited a decreased m-phase areal fraction of ~5-13%.[1]

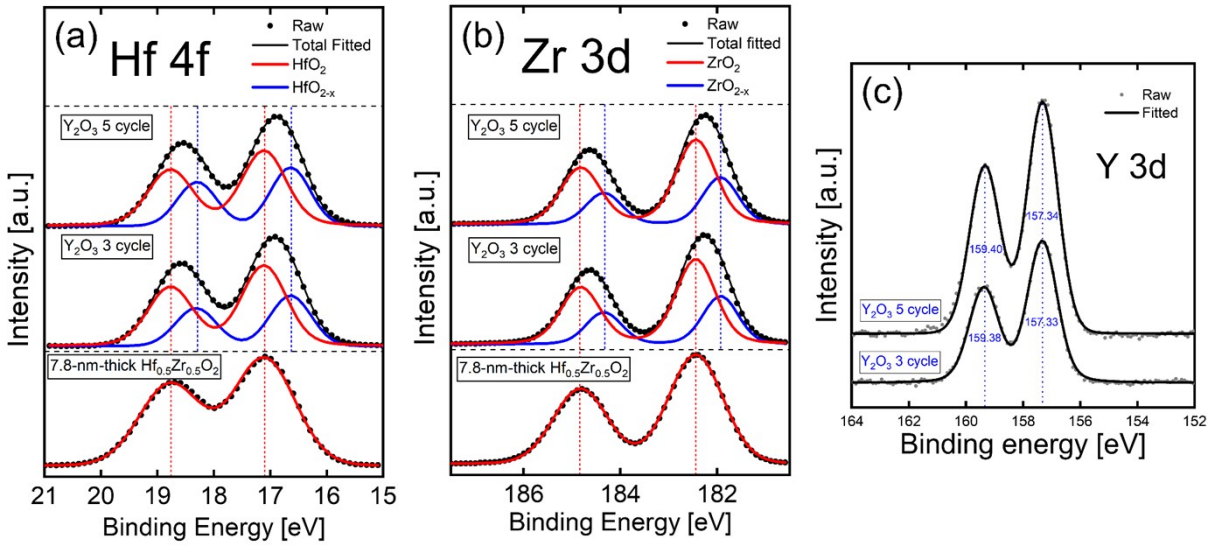

Figure S2. The (a) Hf 4f, (b) Zr 3d, and (c) Y 3d XPS spectra of the undoped 7.8-nm-thick $Hf_{0.5}Zr_{0.5}O_2$ and ~7.8-nm-thick $Hf_{0.5}Zr_{0.5}O_2$ with three and five ALD cycles of Y_2O_3 inserted in the middle of the film. Reproduced with permission.[1] Copyright 2024, Royal Society of Chemistry.

The undoped 7.8-nm-thick $Hf_{0.5}Zr_{0.5}O_2$ film and those with three and five ALD cycles of Y_2O_3 inserted at the middle were analyzed by XPS. The Hf 4f and Zr 3d spectra of the Y-doped films shifted to lower binding energies compared to the undoped film. Deconvolution revealed increased fractions of oxygen-deficient phases (HfO_{2-x} and ZrO_{2-x}), attributed to the substitutional diffusion of Y^{3+} ions into the Hf^{4+} and Zr^{4+}, generating V_O^{2+} to maintain charge neutrality.[1] The Y 3p spectra showed similar binding energies for both three and five Y_2O_3 cycles. Previous studies reported that slightly oxygen-deficient conditions can stabilize the t-phase in HfO_2-based thin films[1, 7-11], consistent with the behavior observed in the Y-diffused samples.

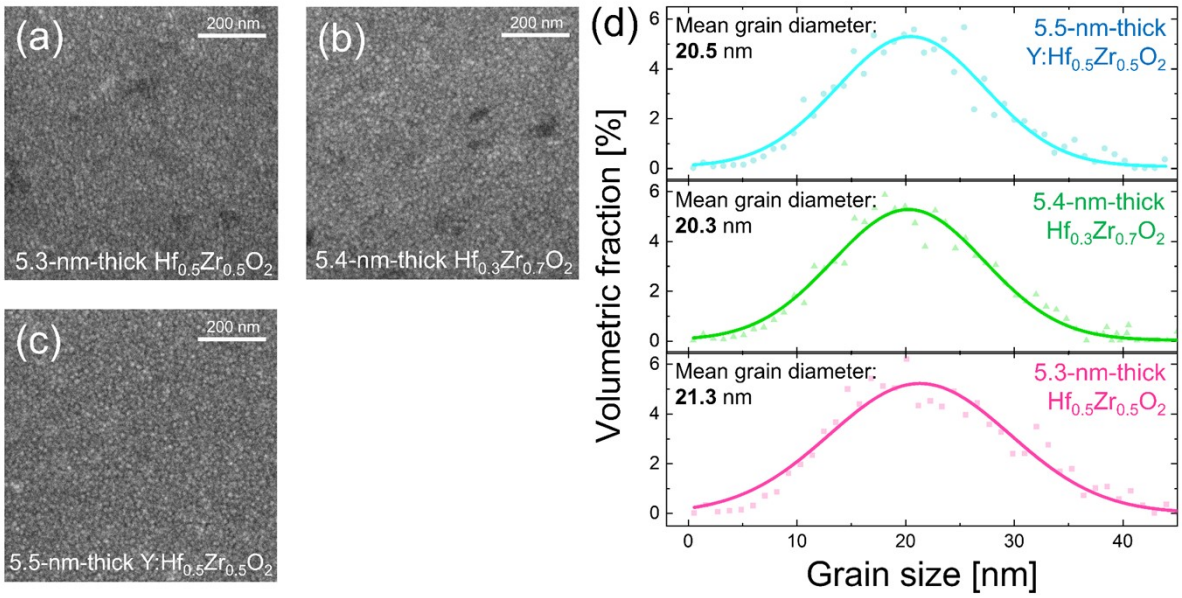

Figure S3. The SEM images of the (a) 5.3-nm-thick $Hf_{0.5}Zr_{0.5}O_2$, (b) 5.4-nm-thick $Hf_{0.3}Zr_{0.7}O_2$, and (c) 5.5-nm-thick $Y:Hf_{0.5}Zr_{0.5}O_2$ films after PDA. (d) Grain diameter distributions and the mean grain diameter of the films analyzed with the watershed method implemented in the Gwyddion software.

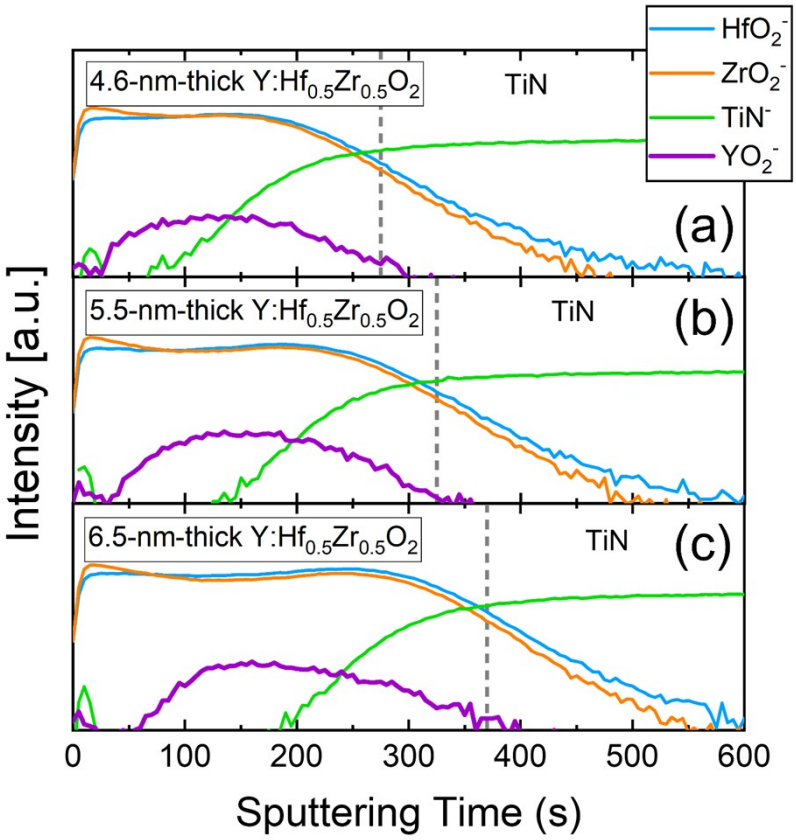

Figure S4. ToF-SIMS depth profiles of the (a) 4.6-nm, (b) 5.5-nm, and (c) 6.5-nm-thick Y:$Hf_{0.5}Zr_{0.5}O_2$ films on TiN bottom electrode after PDA.

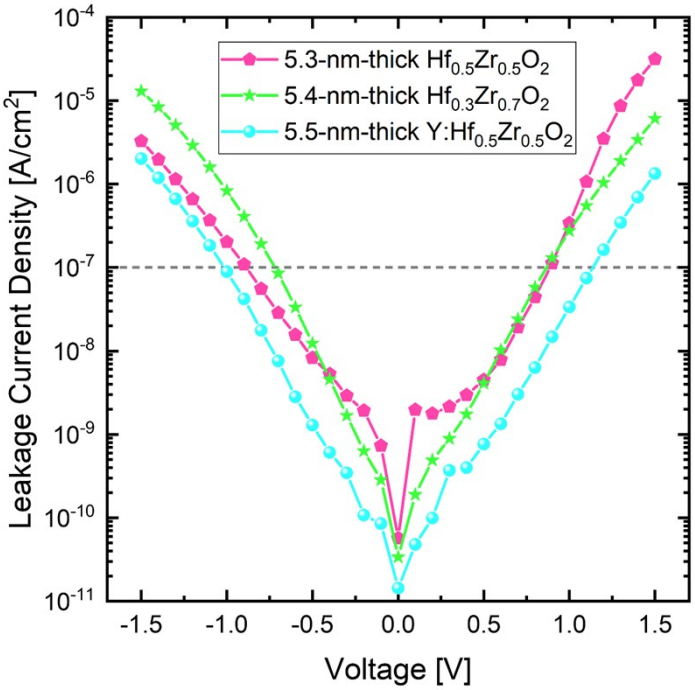

Figure S5. J-V curves of the 5.3-nm-thick $Hf_{0.5}Zr_{0.5}O_2$, 5.4-nm-thick $Hf_{0.3}Zr_{0.7}O_2$, and 5.5-nm-thick $Y:Hf_{0.5}Zr_{0.5}O_2$ films at the pristine state.

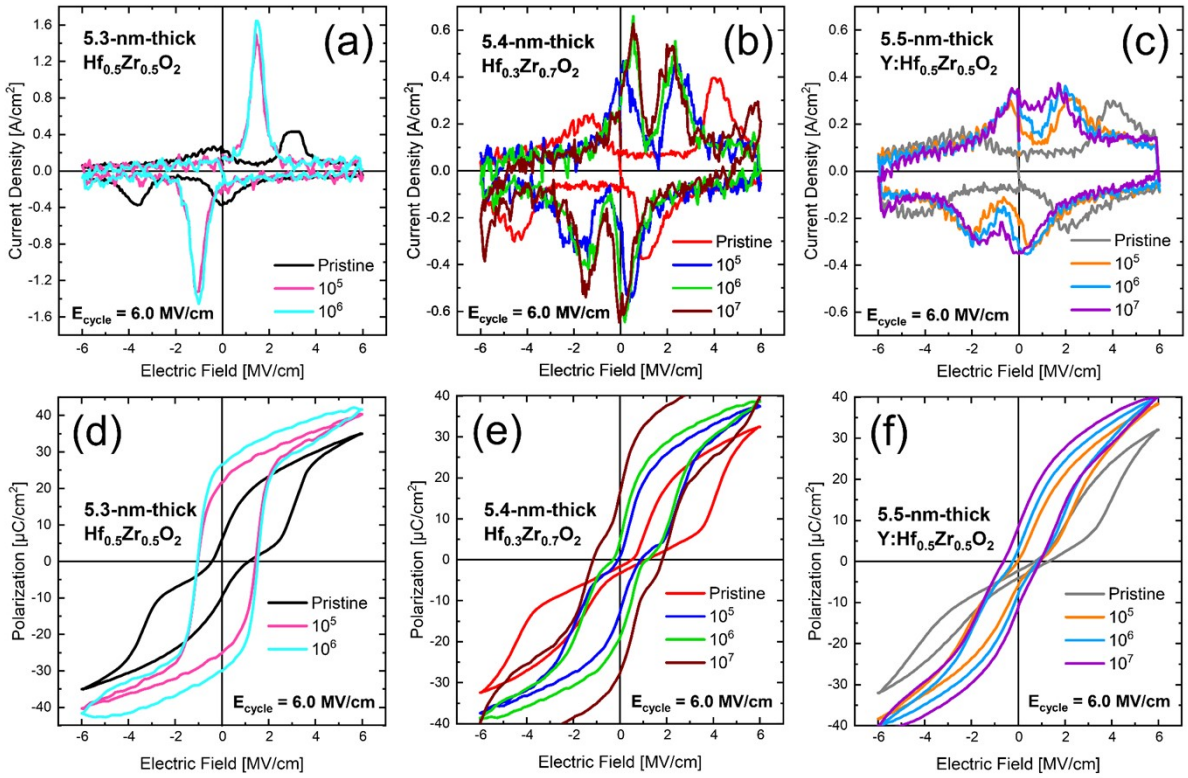

Figure S6. I-E curve changes of the (a) 5.3-nm-thick $Hf_{0.5}Zr_{0.5}O_2$, (b) 5.4-nm-thick $Hf_{0.3}Zr_{0.7}O_2$, and (c) 5.5-nm-thick Y:$Hf_{0.5}Zr_{0.5}O_2$ films with field-cycling at 6.0 MV cm^{-1}. P-E curve changes of the (d) 5.3-nm-thick $Hf_{0.5}Zr_{0.5}O_2$, (e) 5.4-nm-thick $Hf_{0.3}Zr_{0.7}O_2$, and (f) 5.5-nm-thick Y:$Hf_{0.5}Zr_{0.5}O_2$ films with field-cycling at 6.0 MV cm^{-1}.

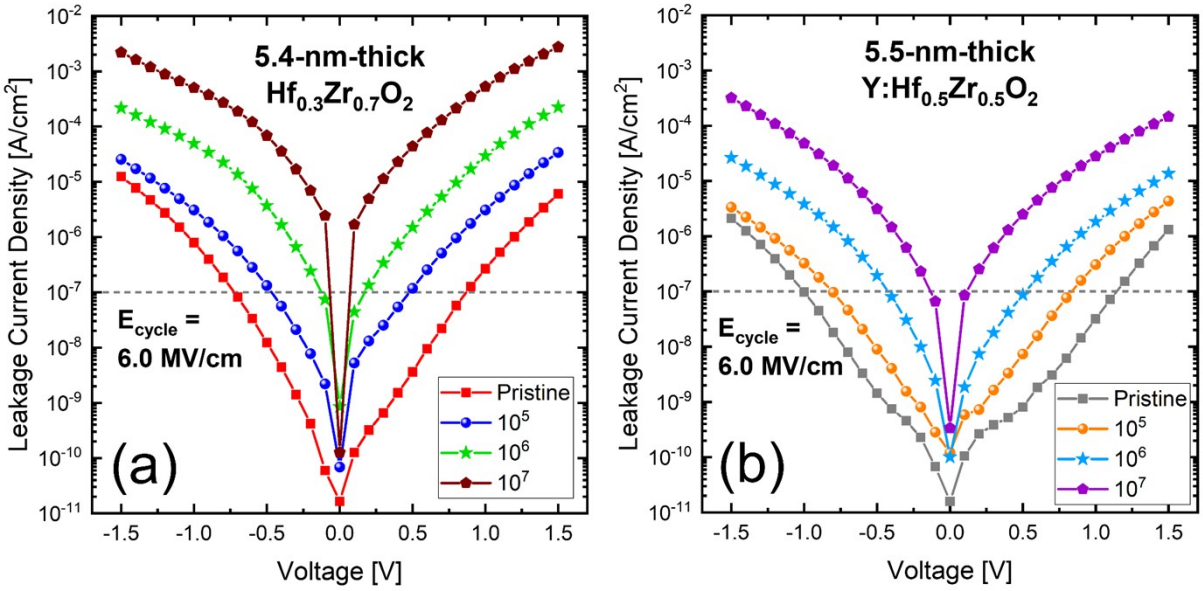

Figure S7. J-V curve changes of the (a) 5.4-nm-thick $Hf_{0.3}Zr_{0.7}O_2$ and (b) 5.5-nm-thick $Y:Hf_{0.5}Zr_{0.5}O_2$ films with field-cycling at 6.0 MV cm^{-1}.

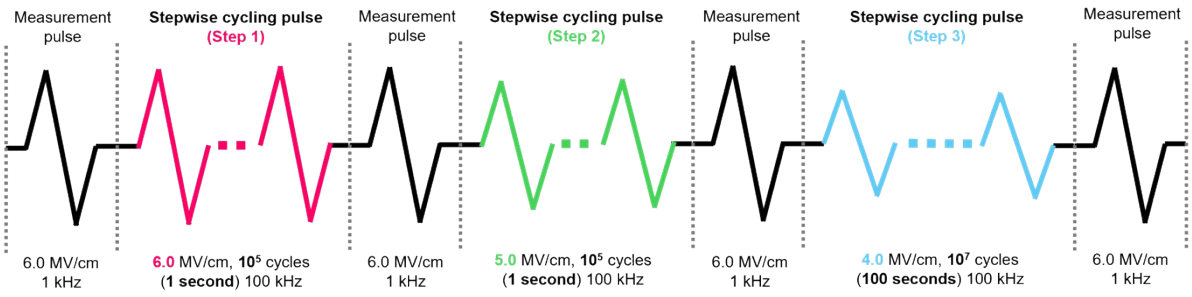

Figure S8. The schematic diagram of the pulse sequences for the stepwise cycling conducted in Figure 4(a)-(d).

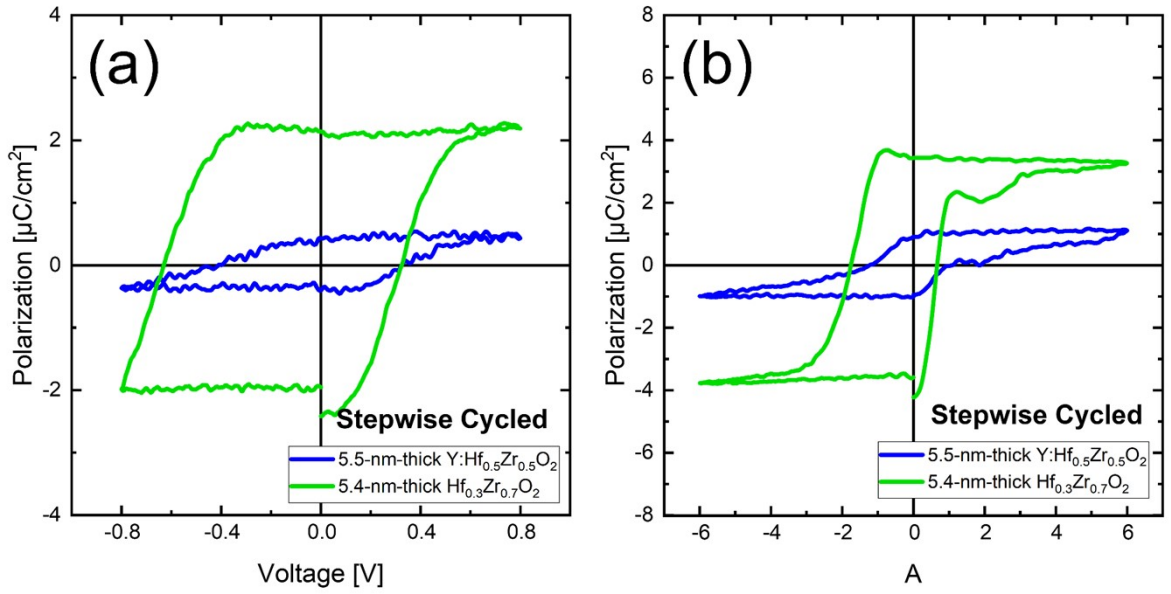

Figure S9. PUND P-V curves of the 5.4-nm-thick $Hf_{0.3}Zr_{0.7}O_2$ and 5.5-nm-thick $Y:Hf_{0.5}Zr_{0.5}O_2$ films after stepwise cycling, adopting (a) 0.8 V and (b) 6 MV cm^{-1} triangular pulses, respectively, with 1 kHz frequency.

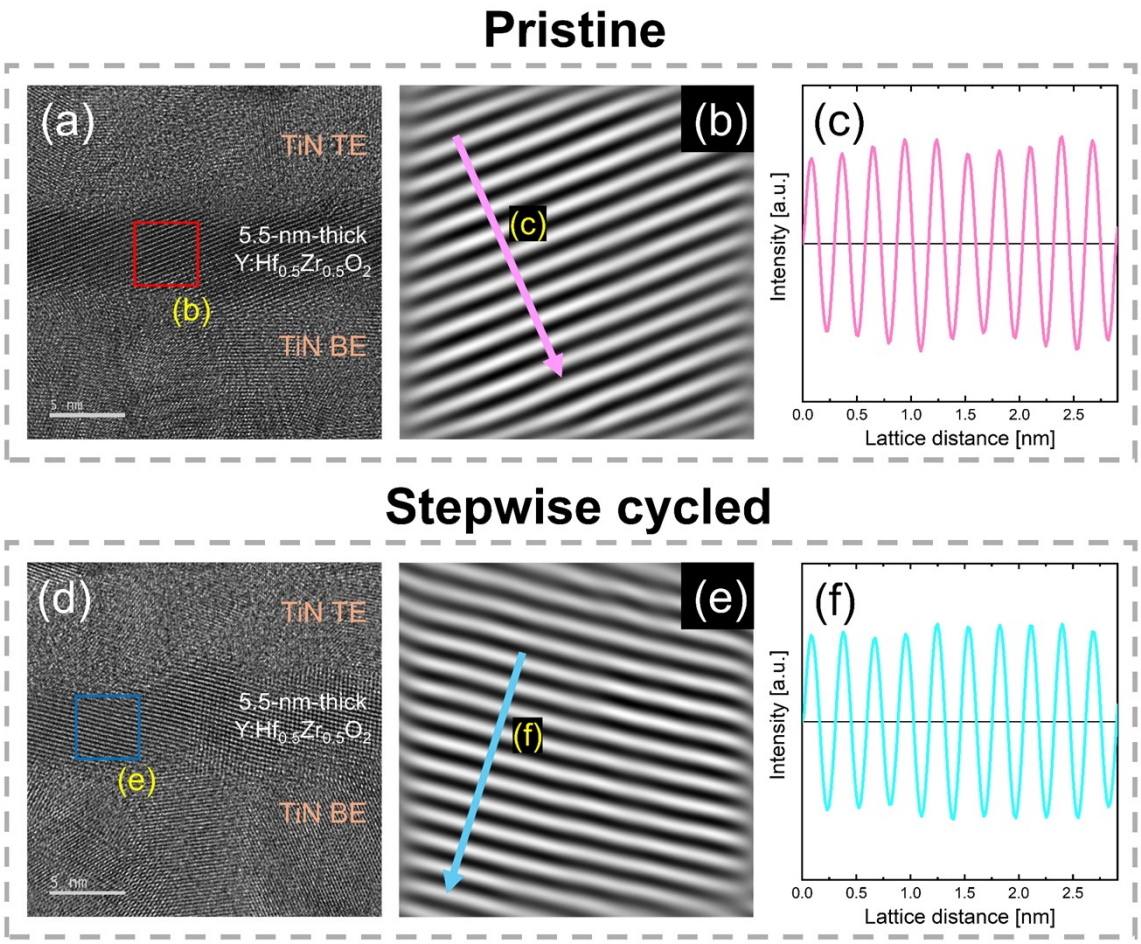

Figure S10. The Cs-TEM images of the 5.5-nm-thick Y:$Hf_{0.5}Zr_{0.5}O_2$ capacitor at the (a) pristine state and (d) after stepwise cycling. The iFFT images for the regions marked with (b) red (pristine) and (e) blue (stepwise cycled) boxes, respectively. The line maps along the (c) pink (pristine) and (f) sky blue (stepwise cycled) arrows, respectively.

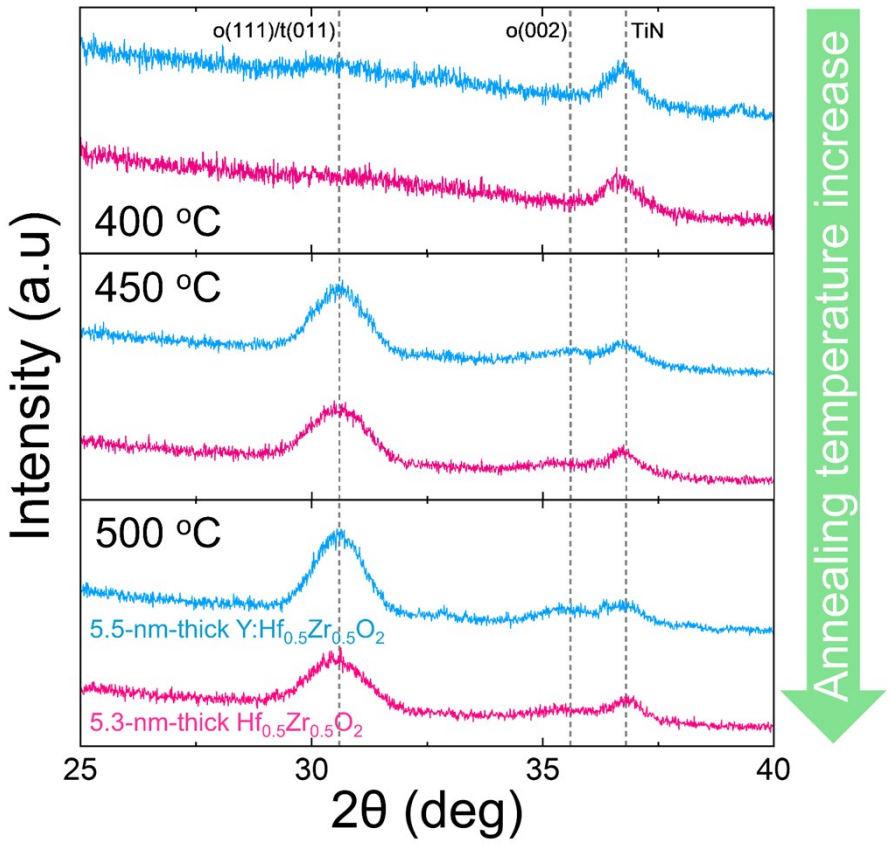

Figure S11. GIXRD patterns (incident angle: 0.5°) of the 5.3-nm-thick $Hf_{0.5}Zr_{0.5}O_2$ (pink) and 5.5-nm-thick $Y:Hf_{0.5}Zr_{0.5}O_2$ (sky blue) films, PMA-treated at 400 °C, 450 °C, and 500 °C, respectively, for 30 seconds.

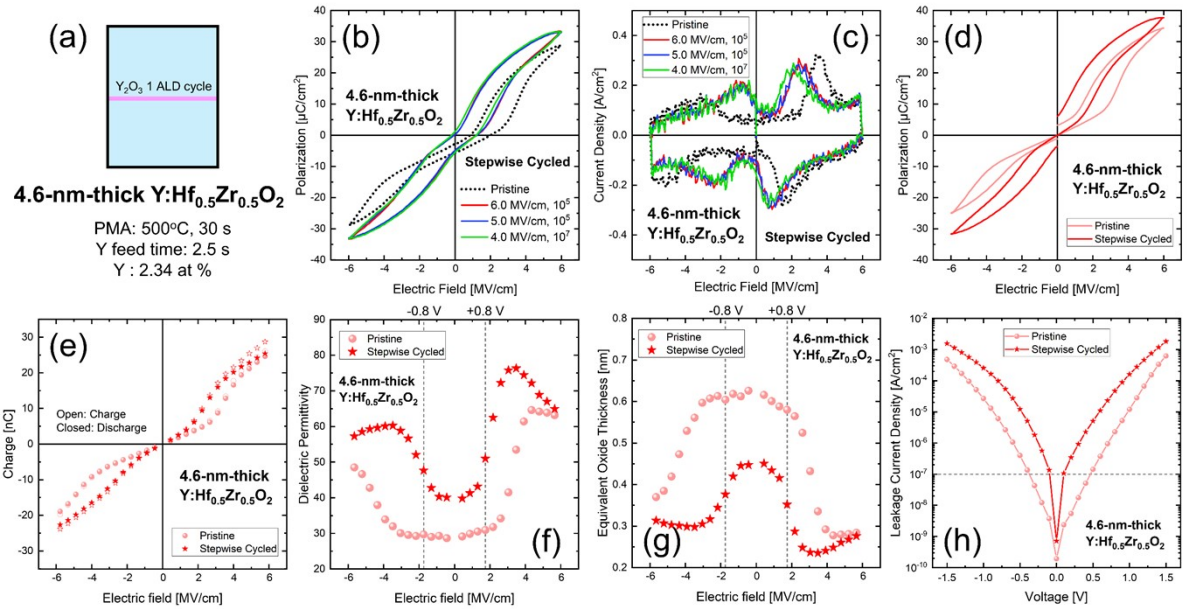

Figure S12. (a) The PMA, Y feeding time, and Y atomic concentration information of the 4.6-nm-thick Y:$Hf_{0.5}Zr_{0.5}O_2$. The (b) P-E and (c) I-E curve changes of the 4.6-nm-thick Y:$Hf_{0.5}Zr_{0.5}O_2$ with stepwise cycling, with cycling sequences of E_{cycle} = 6.0 MV cm^{-1}, 10^5 cycles → E_{cycle} = 5.0 MV cm^{-1}, 10^5 cycles → E_{cycle} = 4.0 MV cm^{-1}, 10^7 cycles. The (d) non-switching P-E curves, (e) Q_c (open) and Q_d (closed) characteristics, (f) *k*-E curves, (g) EOT-E curves, and (h) J-V curves of the 4.6-nm-thick Y:$Hf_{0.5}Zr_{0.5}O_2$, respectively, at the pristine state and after stepwise cycling.

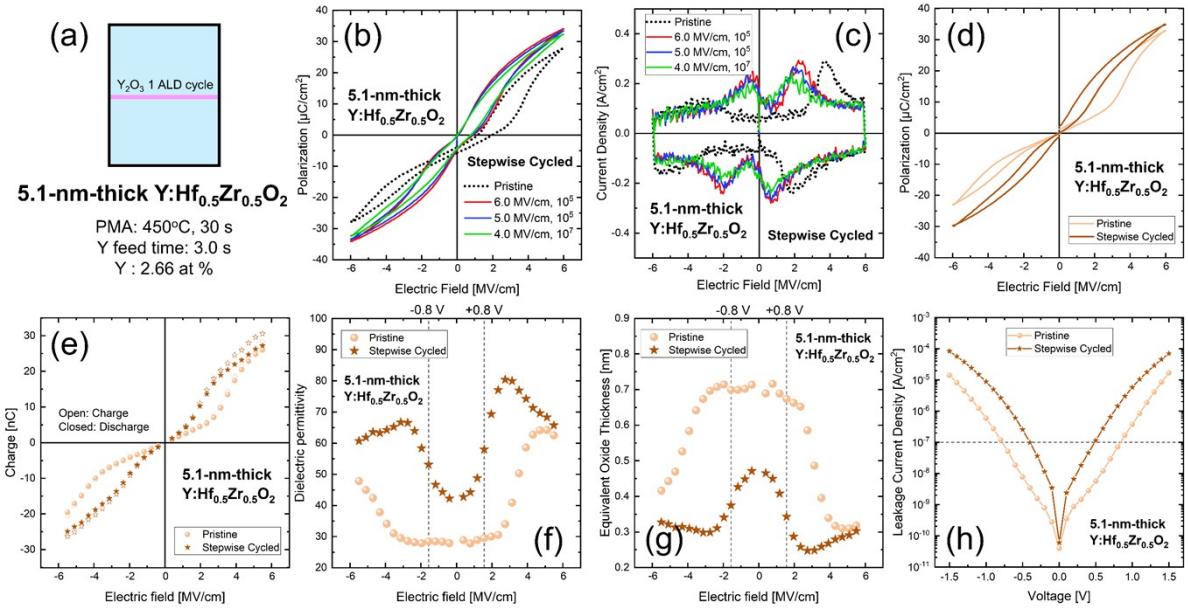

Figure S13. (a) The PMA, Y feeding time, and Y atomic concentration information of the 5.1-nm-thick Y:$Hf_{0.5}Zr_{0.5}O_2$. The (b) P-E and (c) I-E curve changes of the 5.1-nm-thick Y:$Hf_{0.5}Zr_{0.5}O_2$ with stepwise cycling, with cycling sequences of E_{cycle} = 6.0 MV cm^{-1}, 10^5 cycles → E_{cycle} = 5.0 MV cm^{-1}, 10^5 cycles → E_{cycle} = 4.0 MV cm^{-1}, 10^7 cycles. The (d) non-switching P-E curves, (e) Q_c (open) and Q_d (closed) characteristics, (f) *k*-E curves, (g) EOT-E curves, and (h) J-V curves of the 5.1-nm-thick Y:$Hf_{0.5}Zr_{0.5}O_2$, respectively, at the pristine state and after stepwise cycling.

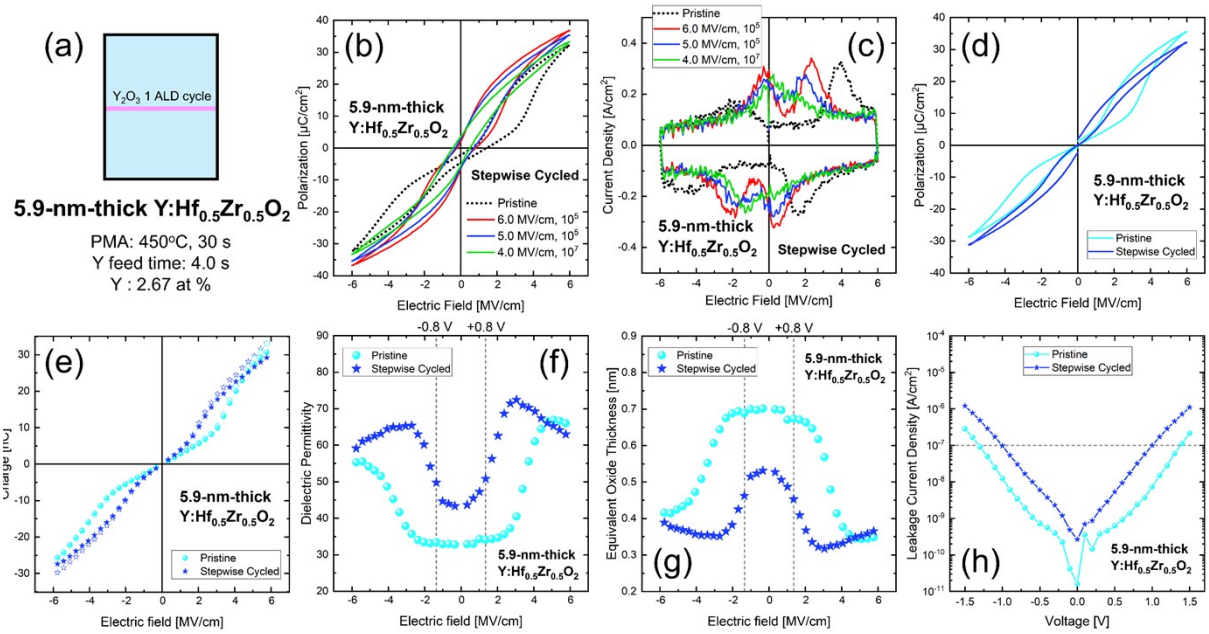

Figure S14. (a) The PMA, Y feeding time, and Y atomic concentration information of the 5.9-nm-thick Y:$Hf_{0.5}Zr_{0.5}O_2$. The (b) P-E and (c) I-E curve changes of the 5.9-nm-thick Y:$Hf_{0.5}Zr_{0.5}O_2$ with stepwise cycling, with cycling sequences of E_{cycle} = 6.0 MV cm^{-1}, 10^5 cycles → E_{cycle} = 5.0 MV cm^{-1}, 10^5 cycles → E_{cycle} = 4.0 MV cm^{-1}, 10^7 cycles. The (d) non-switching P-E curves, (e) Q_c (open) and Q_d (closed) characteristics, (f) *k*-E curves, (g) EOT-E curves, and (h) J-V curves of the 5.9-nm-thick Y:$Hf_{0.5}Zr_{0.5}O_2$, respectively, at the pristine state and after stepwise cycling.

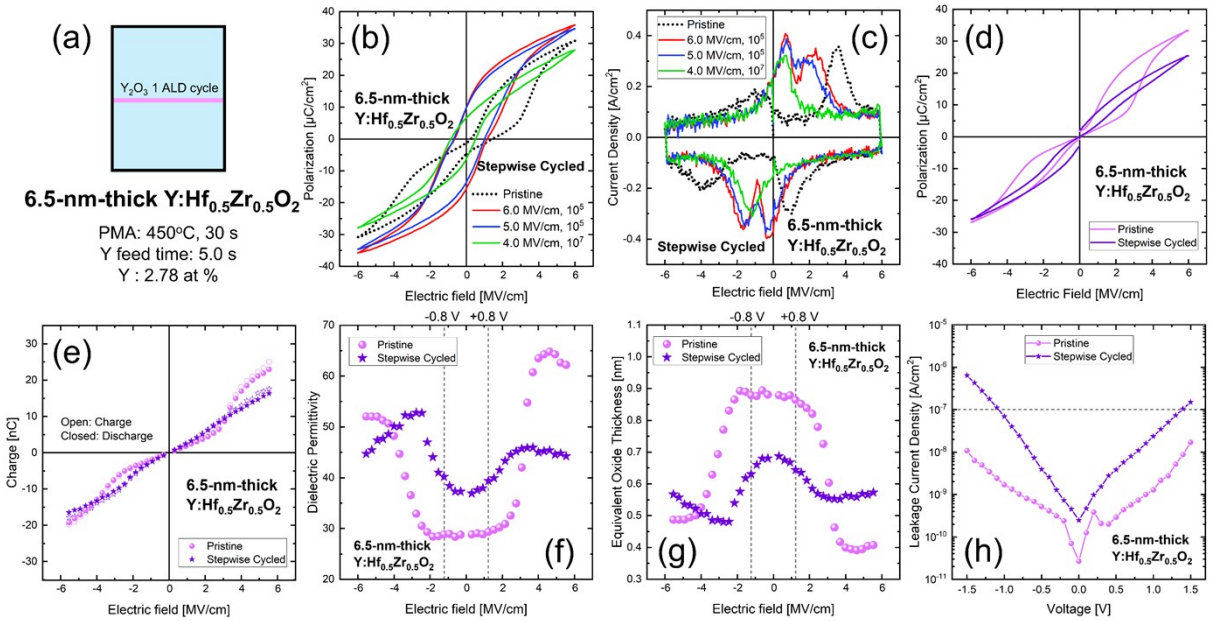

Figure S15. (a) The PMA, Y feeding time, and Y atomic concentration information of the 6.5-nm-thick Y:$Hf_{0.5}Zr_{0.5}O_2$. The (b) P-E and (c) I-E curve changes of the 6.5-nm-thick Y:$Hf_{0.5}Zr_{0.5}O_2$ with stepwise cycling, with cycling sequences of E_{cycle} = 6.0 MV cm^{-1}, 10^5 cycles → E_{cycle} = 5.0 MV cm^{-1}, 10^5 cycles → E_{cycle} = 4.0 MV cm^{-1}, 10^7 cycles. The (d) non-switching P-E curves, (e) Q_c (open) and Q_d (closed) characteristics, (f) *k*-E curves, (g) EOT-E curves, and (h) J-V curves of the 6.5-nm-thick Y:$Hf_{0.5}Zr_{0.5}O_2$, respectively, at the pristine state and after stepwise cycling.

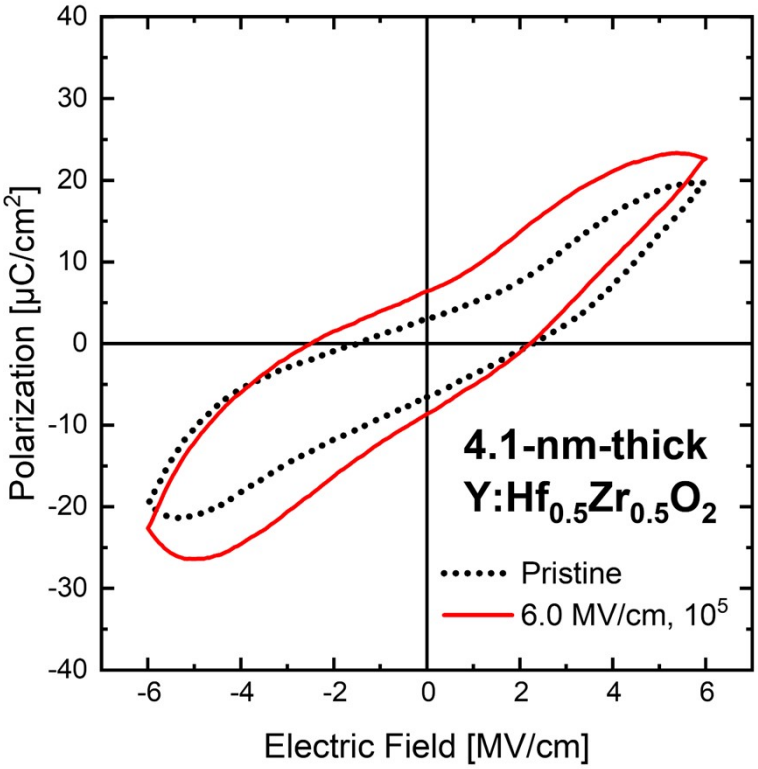

Figure S16. P-E curve changes of the 4.1-nm-thick Y:$Hf_{0.5}Zr_{0.5}O_2$ film with field-cycling at 6.0 MV cm^{-1} for 10^5 cycles.

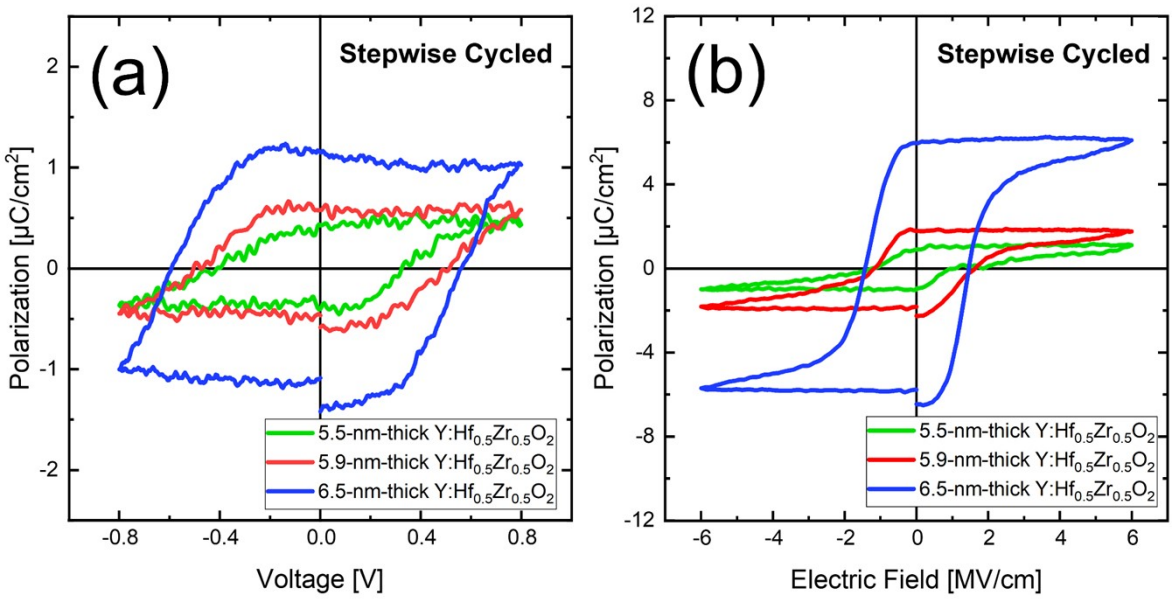

Figure S17. PUND P-V curves of the 5.5-nm, 5.9-nm, and 6.5-nm-thick Y: $Hf_{0.5}Zr_{0.5}O_2$ films after stepwise cycling, adopting (a) 0.8 V and (b) 6 MV cm^{-1} triangular pulses, respectively, with 1 kHz frequency.

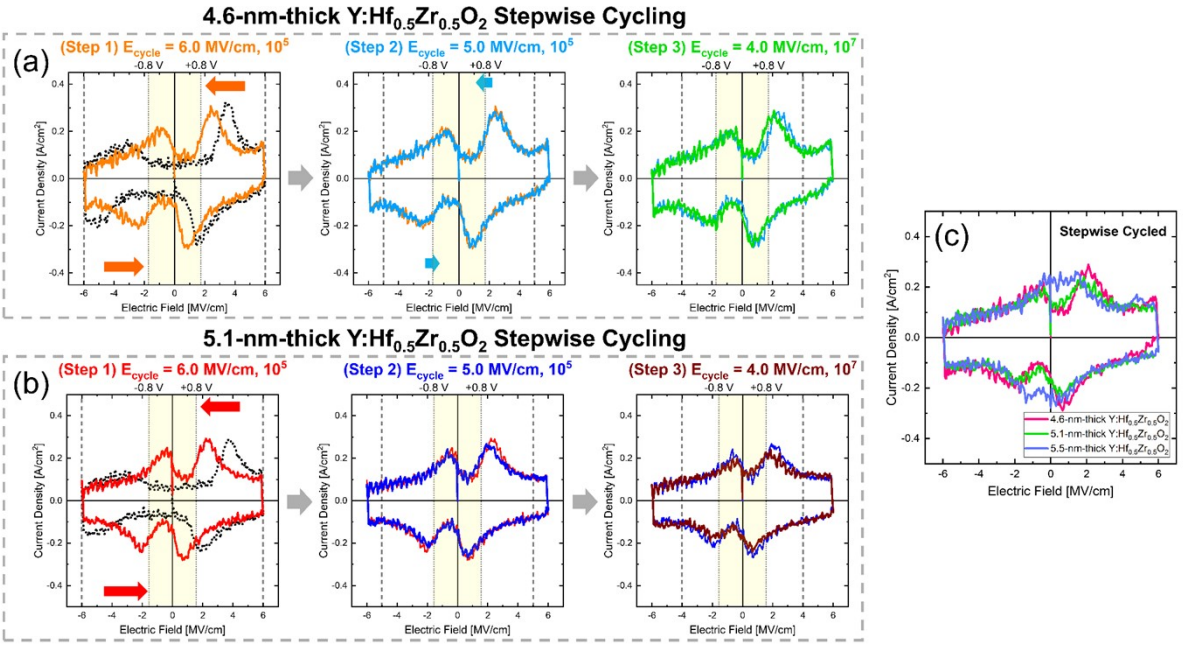

Figure S18. I-E curve changes of the (a) 4.6-nm-thick $Y:Hf_{0.5}Zr_{0.5}O_2$ and (b) 5.1-nm-thick $Y:Hf_{0.5}Zr_{0.5}O_2$ films with stepwise cycling after sequential cycling steps of (step 1) E_{cycle} = 6.0 MV cm^{-1}, 10^5 cycles → (step 2) E_{cycle} = 5.0 MV cm^{-1}, 10^5 cycles → (step 3) E_{cycle} = 4.0 MV cm^{-1}, 10^7 cycles. (c) The I-E curves of the 4.6-nm, 5.1-nm, and 5.5-nm-thick $Y:Hf_{0.5}Zr_{0.5}O_2$ films after stepwise cycling.

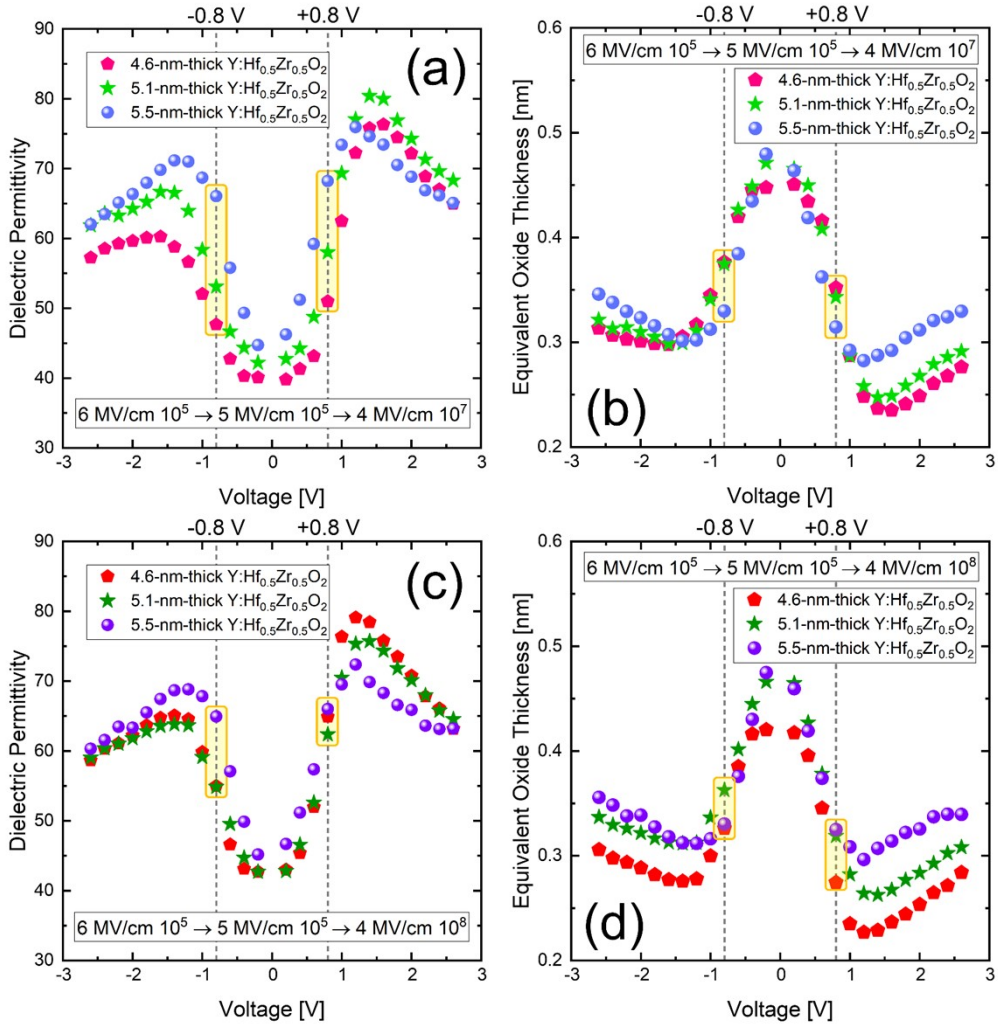

Figure S19. The (a) *k*-E and (b) EOT-E curves of the 4.6-nm, 5.1-nm, and 5.5-nm-thick Y:$Hf_{0.5}Zr_{0.5}O_2$ films after stepwise cycling with sequential cycling steps of E_{cycle} = 6.0 MV cm^{-1}, 10^5 cycles → E_{cycle} = 5.0 MV cm^{-1}, 10^5 cycles → E_{cycle} = 4.0 MV cm^{-1}, 10^7 cycles. The (c) *k*-E and (d) EOT-E curves of the 4.6-nm, 5.1-nm, and 5.5-nm-thick Y:$Hf_{0.5}Zr_{0.5}O_2$ films after stepwise cycling with sequential cycling steps of E_{cycle} = 6.0 MV cm^{-1}, 10^5 cycles → E_{cycle} = 5.0 MV cm^{-1}, 10^5 cycles → E_{cycle} = 4.0 MV cm^{-1}, 10^8 cycles.

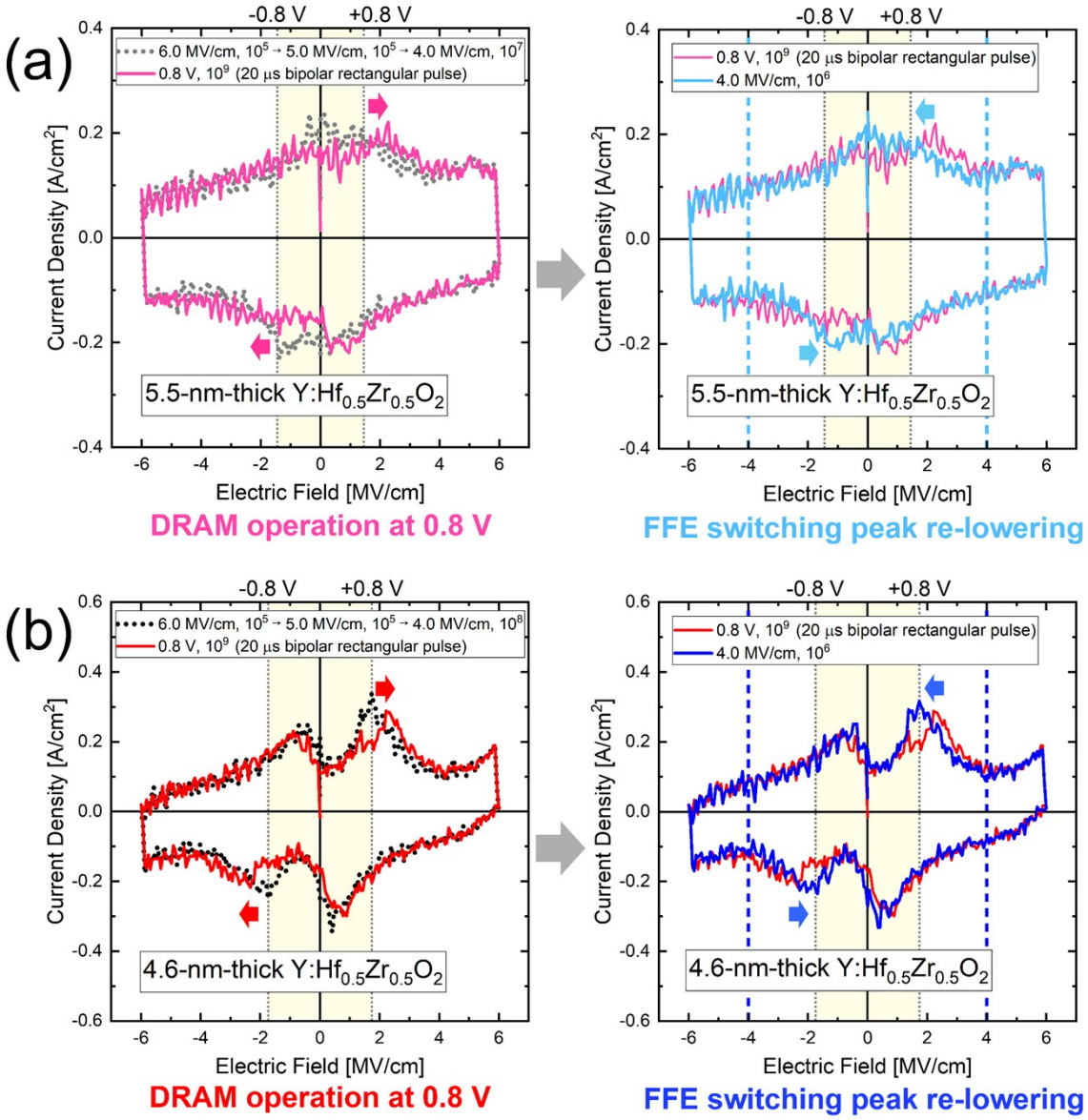

Figure S20. (a) I-E curve changes of the 5.5-nm-thick Y:$Hf_{0.5}Zr_{0.5}O_2$ film stepwise cycled with sequential cycling steps of 100 kHz bipolar triangular pulses at E_{cycle} = 6.0 MV cm^{-1}, 10^5 cycles → E_{cycle} = 5.0 MV cm^{-1}, 10^5 cycles → E_{cycle} = 4.0 MV cm^{-1}, 10^7 cycles (dotted grey). Subsequently, bipolar rectangular pulses of 0.8 V with 20 μs width were applied for 10^9 cycles (pink), followed by 100 kHz bipolar triangular pulses at 4.0 MV cm^{-1}, 10^6 cycles (sky blue). (b) I-E curve changes of the 4.6-nm-thick Y:$Hf_{0.5}Zr_{0.5}O_2$ film stepwise cycled with sequential cycling steps of 100 kHz bipolar triangular pulses at E_{cycle} = 6.0 MV cm^{-1}, 10^5 cycles → E_{cycle} = 5.0 MV cm^{-1}, 10^5 cycles → E_{cycle} = 4.0 MV cm^{-1}, 10^8 cycles (dotted black). Subsequently, bipolar rectangular pulses of 0.8 V with 20 μs width were applied for 10^9 cycles (red), followed by 100 kHz bipolar triangular pulses at 4.0 MV cm^{-1}, 10^6 cycles (blue).

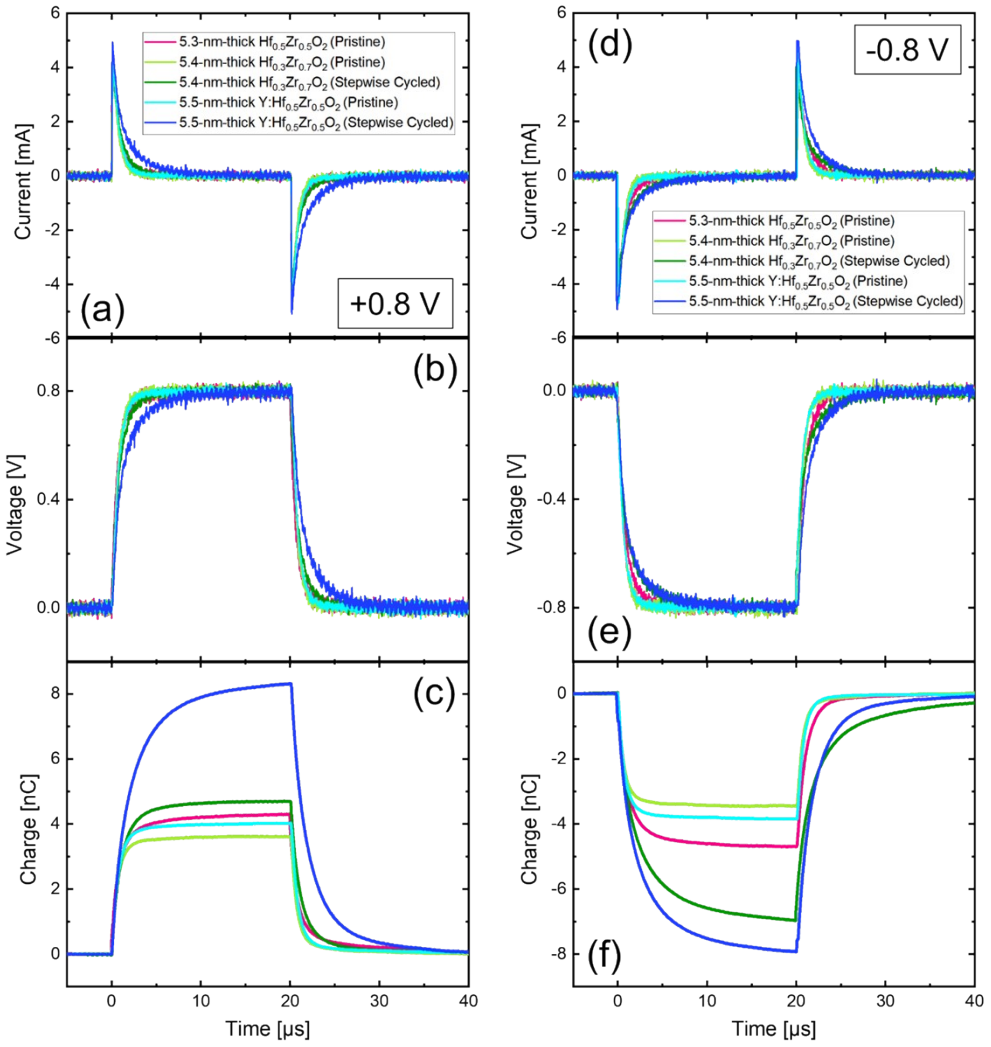

Figure S21. The transient (a) current-time, (b) voltage-time, and (c) charge-time curves of the 5.3-nm-thick $Hf_{0.5}Zr_{0.5}O_2$ (pristine), 5.4-nm-thick $Hf_{0.3}Zr_{0.7}O_2$ (pristine and stepwise cycled), and 5.5-nm-thick $Y:Hf_{0.5}Zr_{0.5}O_2$ (pristine and stepwise cycled) films, respectively, under a rectangular applied pulse with a +0.8 V height and a 20 μs length. The transient (d) current-time, (e) voltage-time, and (f) charge-time curves of the 5.3-nm-thick $Hf_{0.5}Zr_{0.5}O_2$ (pristine), 5.4-nm-thick $Hf_{0.3}Zr_{0.7}O_2$ (pristine and stepwise cycled), and 5.5-nm-thick $Y:Hf_{0.5}Zr_{0.5}O_2$ (pristine and stepwise cycled) films, respectively, under a rectangular applied pulse with a -0.8 V height and a 20 μs length.

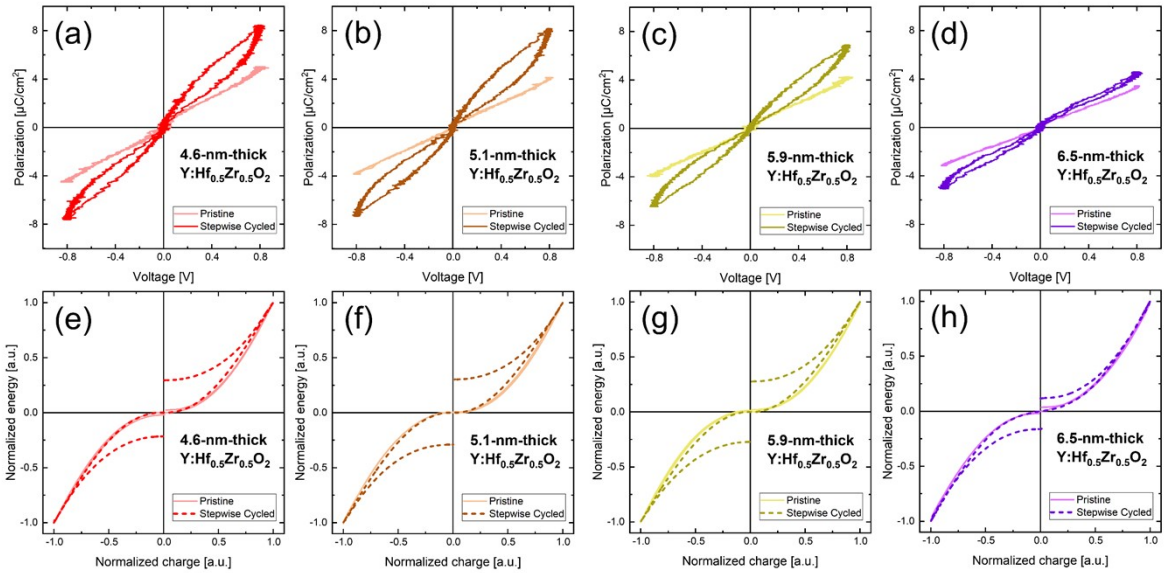

Figure S22. The calculated polarization-voltage curves of the (a) 4.6-nm, (b) 5.1-nm, (c) 5.9-nm, and (d) 6.5-nm-thick Y:$Hf_{0.5}Zr_{0.5}O_2$ films, respectively, at the pristine state and after stepwise cycling. The normalized energy-charge curves during charging and discharging of the (a) 4.6-nm, (b) 5.1-nm, (c) 5.9-nm, and (d) 6.5-nm-thick Y:$Hf_{0.5}Zr_{0.5}O_2$ films, respectively, at the pristine state and after stepwise cycling.

Table S1. The energy loss values of the 4.6-nm, 5.1-nm, 5.9-nm, and 6.5-nm-thick Y:$Hf_{0.5}Zr_{0.5}O_2$ films for the pristine state and after stepwise cycling at ±0.8 V.

		4.6-nm-thick Y:$Hf_{0.5}Zr_{0.5}O_2$		5.1-nm-thick Y:$Hf_{0.5}Zr_{0.5}O_2$		5.9-nm-thick Y:$Hf_{0.5}Zr_{0.5}O_2$		6.5-nm-thick Y:$Hf_{0.5}Zr_{0.5}O_2$	
		Pristine	Stepwise cycled	Pristine	Stepwise cycled	Pristine	Stepwise cycled	Pristine	Stepwise cycled
Energy loss (%)	+0.8 V	2.2	29.4	0.5	30.2	2.0	27.6	3.4	11.4
	-0.8 V	1.7	21.5	0.0	29.1	1.4	27.2	2.0	15.9

References

1. J. Shin, H. Seo, K. H. Ye, Y. H. Jang, D. S. Kwon, J. Lim, T. K. Kim, H. Paik, H. Song and H. N. Kim, *J. Mater. Chem. C*, 2024, **12**, 5035-5046.
2. M. H. Park, H. J. Kim, Y. J. Kim, T. Moon and C. S. Hwang, *Appl. Phys. Lett.*, 2014, **104**.
3. H. J. Kim, M. H. Park, Y. J. Kim, Y. H. Lee, W. Jeon, T. Gwon, T. Moon, K. D. Kim and C. S. Hwang, *Appl. Phys. Lett.*, 2014, **105**.
4. M. H. Park, H. J. Kim, Y. J. Kim, Y. H. Lee, T. Moon, K. D. Kim, S. D. Hyun and C. S. Hwang, *Appl. Phys. Lett.*, 2015, **107**.
5. M. H. Park, T. Schenk, C. M. Fancher, E. D. Grimley, C. Zhou, C. Richter, J. M. LeBeau, J. L. Jones, T. Mikolajick and U. Schroeder, *J. Mater. Chem. C*, 2017, **5**, 4677-4690.
6. M. H. Park, C. C. Chung, T. Schenk, C. Richter, K. Opsomer, C. Detavernier, C. Adelmann, J. L. Jones, T. Mikolajick and U. Schroeder, *Adv. Electron. Mater.*, 2018, **4**, 1800091.
7. Y. H. Lee, H. J. Kim, T. Moon, K. Do Kim, S. D. Hyun, H. W. Park, Y. B. Lee, M. H. Park and C. S. Hwang, *Nanotechnology*, 2017, **28**, 305703.
8. W. Hamouda, A. Pancotti, C. Lubin, L. Tortech, C. Richter, T. Mikolajick, U. Schroeder and N. Barrett, *J. Appl. Phys.*, 2020, **127**.
9. M. Materano, P. D. Lomenzo, A. Kersch, M. H. Park, T. Mikolajick and U. Schroeder, *Inorg. Chem. Front.*, 2021, **8**, 2650-2672.
10. T. Mittmann, T. Szyjka, H. Alex, M. C. Istrate, P. D. Lomenzo, L. Baumgarten, M. Müller, J. L. Jones, L. Pintilie and T. Mikolajick, *Phys. Status Solidi - Rapid Res. Lett.*, 2021, **15**, 2100012.
11. U. Schroeder, M. H. Park, T. Mikolajick and C. S. Hwang, *Nat. Rev. Mater.*, 2022, **7**, 653-669.